JOURNAL OF COMPUTATIONAL PHYSICS 121, 298–313 (1995)

The Numerical Integration of the Vlasov Equation Possessing an Invariant

G. MANFREDI, M. SHOUCRI, M. R. FEIX,* P. BERTRAND,† E. FIJALKOW,* AND A. GHIZZO†

Centre Canadien de Fusion Magnétique, Varennes, Québec, Canada J3X 1S1

Received September 27, 1994; revised February 14, 1995

A new method for the numerical integration of the Vlasov equation is presented, which can be applied whenever its characteristics possess an exact invariant. It consists in expressing the distribution function in terms of the invariant itself. The dimensionality of the phase space is thus reduced of one unity, since the invariant only appears as a label of the Vlasov equation and can be coarsely discretized. This technique is applied to the study of the Kelvin–Helmoltz instability, with a very limited number of invariants. Subsequently an example of ion-temperature-gradient instability is analyzed. Although a larger number of invariants are required to describe the temperature profile, qualitatively correct results can be obtained with fewer invariants. Test particles are used to illustrate stochastic diffusion in the phase space and to calculate the diffusion coefficients.

1. INTRODUCTION

The numerical integration of the Vlasov equation is one of the key challenges of computational plasma physics. Since the early days of this discipline, an intense work on this subject has produced many different numerical schemes, which, however, can be bunched together in two main groups. On the one hand, particle-in-cell (PIC) codes have proven to be useful in studying plasma dynamics even for two- and three-dimensional problems and complex geometries. However, it is generally recognized that PIC codes present a high level of numerical noise, especially in regions of phase space where the density is low. On the other hand, eulerian Vlasov codes [1, 2] display an extremely low level of numerical noise and prove to be able to describe fine vortex structures in phase space. Unfortunately, eulerian codes demand a stronger numerical effort than their PIC counterparts, for they require the discretization of the whole phase space. For this reason, most of the problems so far treated with eulerian codes are one-dimensional in space. Recently, an eulerian code has been developed which is three-dimensional in phase space (two spatial and one velocity coordinates) [3]. This code solves the drift-kinetic or guiding center Vlasov equation, which couples $\mathbf{E} \times \mathbf{B}$ motion across a magnetic field to the motion parallel to the magnetic field. Such a model is relevant to the study of real plasmas in strong magnetic fields, in which the $\mathbf{E} \times \mathbf{B}$ drift plays a determinant role, e.g., the problem of plasma confinement and anomalous diffusion across the magnetic field, or the study of instabilities at the edge of a tokamak [4, 5]. Several interesting results, concerning Kelvin–Helmoltz (KH) and ion-temperature-gradient (ITG) instabilities, have been obtained by means of this code.

The aim of the present paper is to propose a method that drastically decreases the computational effort of eulerian codes and to apply this method to the drift kinetic equation. The method can be applied whenever the characteristics of the Vlasov equation possess an exact invariant and consists in expressing the distribution function in terms of this invariant. The key point is that very good results (both qualitatively and quantitatively) can be obtained with a rough sampling of the invariant.

The paper is organized as follows. In Section 2 we present the basics of the method. In Section 3 we apply it to the solution of the drift-kinetic Vlasov equation, and give details of the numerical algorithm. Numerical results are presented in Section 4, for the study of the KH instability, and in Section 5, for the simulation of the ITG mode. In Section 6 we conclude and discuss the application of our method to other physically relevant situations.

2. THE INVARIANT METHOD

In order to clearly illustrate the essence of this technique, we start from a very simple example. Let us consider the Vlasov equation with a potential $\phi(x)$:

$$\frac{\partial f}{\partial t} + v\frac{\partial f}{\partial x} - \frac{\partial \phi}{\partial x}\frac{\partial f}{\partial v} = 0. \tag{1}$$

The invariant is, of course, the energy: $I(x, v) = v^2/2 + \phi(x)$ and we have $\dot{I} = \partial I/\partial t + (\partial I/\partial x)\dot{x} + (\partial I/\partial v)\dot{v} = 0$. Note that, in this simple case, I is both an invariant of the characteristics and a global invariant: the former property, as

* URA D1803, CNRS-Université d'Orléans, France.
† LPMI-URA835, CNRS-Université de Nancy, France.

0021-9991/95 $12.00

it will appear later, is the fundamental one. Now, we express f as a function of x, I, and t:

$$f(x, v, t) = F(x, I, t). \tag{2}$$

Calculating the derivatives of F, for example,

$$\frac{\partial f}{\partial t} = \frac{\partial F}{\partial t} + \frac{\partial F}{\partial I}\frac{\partial I}{\partial t},$$

we obtain the equation for F, which reads

$$\frac{\partial F}{\partial t} + v\frac{\partial F}{\partial x} + \frac{\partial F}{\partial I}\left(\frac{\partial I}{\partial t} + v\frac{\partial I}{\partial x} - \frac{\partial \phi}{\partial x}\frac{\partial I}{\partial v}\right) = 0. \tag{3}$$

But the last term in parenthesis is just $\dot{I} = 0$. Thus, further expressing v as a function of x, I, and t,

$$v = \sqrt{2(I - \phi(x))} \equiv G(x, I),$$

Eq. (3) finally becomes

$$\frac{\partial F}{\partial t} + G(x, I)\frac{\partial F}{\partial x} = 0. \tag{4}$$

Now, we see that in Eq. (4), the invariant I is nothing but a (continuous) label. Although the new phase space (x, I) is still two-dimensional, no differential operation is carried out on the variable I. For this reason, when discretizing Eq. (4), we can take a small number of values of I, without affecting the accuracy of the numerical integration. The sole source of error concerning the I variable will come from the limited precision with which one can describe the initial condition. If we keep N invariants, we shall solve N *decoupled* equations, each one for a value of I,

$$\frac{\partial F_j}{\partial t} + G_j(x)\frac{\partial F_j}{\partial x} = 0, \quad j = 1, N, \tag{5}$$

where $F_j(x, t) = F(x, I_j, t)$ and $G_j(x) = G(x, I_j)$. What we actually do, is to bunch together particles with the same I (the same energy), and subsequently let each group evolve independently. Note that this philosophy is somehow reminiscent of the multiple water-bag method [6], in which the choice of a special initial condition (the sum of several plateau functions) allows us to reduce the Vlasov equation to a set of hydrodynamic-like equations.

Finally, we note that, for a fully self-consistent problem, the N "species" F_j in Eq. (5) will, of course, be coupled through the Poisson equation.

3. THE DRIFT-KINETIC VLASOV MODEL

In this section we present the basic equations that govern the plasma dynamics in the case of a uniform magnetic field $\mathbf{B} = (B_x, 0, B_z)$ in the (x, z) plane making an angle θ with the x axis. For a strong magnetic field the $\mathbf{E} \times \mathbf{B}$ drift is the dominant one across the magnetic field. Therefore, we write the velocity as

$$\mathbf{v} = \mathbf{v}_\parallel + \mathbf{v}_\perp \quad \text{with } \mathbf{v}_\perp = \mathbf{E} \times \mathbf{B}/B^2.$$

The drift-kinetic Vlasov equation reads

$$\frac{\partial f_{i,e}}{\partial t} + \mathbf{v}_\parallel \cdot \nabla_\parallel f_{i,e} + \frac{\mathbf{E} \times \mathbf{B}}{B^2} \cdot \nabla_\perp f_{i,e} \pm \frac{q}{m_{i,e}} \mathbf{E}_\parallel \cdot \frac{\partial f_{i,e}}{\partial v_\parallel} = 0. \tag{6}$$

We further suppose a homogeneous plasma in the z direction, thus reducing the electron and ion distribution functions to functions of three variables: $f_{i,e}(x, y, v_\parallel)$, x being the periodic space variable, y the nonperiodic one, and $v_\parallel$ the velocity parallel to the magnetic field. The geometry of the computational box is shown in Fig. 1: the spatial domain is rectangular with $0 \le x \le L_x$ and $-L_y \le y \le L_y$. We shall also assume the ion mass to be much larger than the electron mass. In this case, Eq. (6) can be integrated over $v_\parallel$ to give a hydrodynamic equation for the ion density $n_i(x, y, t)$. We shall see later on that this assumption just means that we only keep one invariant, namely $I = 0$, for the ions. Thus, the electron equation becomes, neglecting the subscript e for the electrons,

$$\frac{\partial f}{\partial t} + \left(v_\parallel \cos\theta + \frac{E_y}{B}\sin\theta\right)\frac{\partial f}{\partial x} - \frac{E_x}{B}\sin\theta\frac{\partial f}{\partial y} - \frac{qE_x}{m}\cos\theta\frac{\partial f}{\partial v_\parallel} = 0 \tag{7}$$

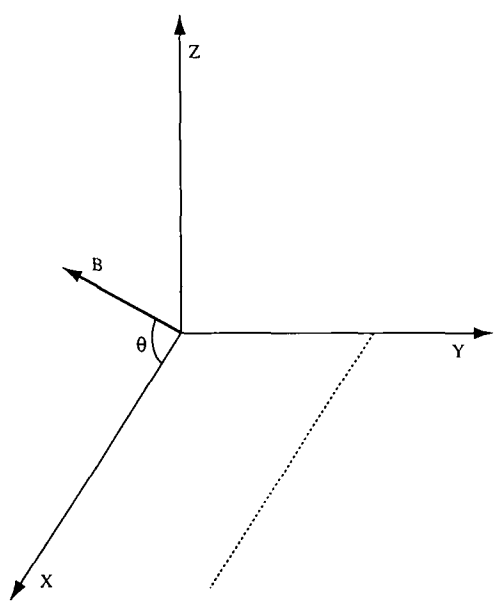

FIG. 1. Geometry of the computational box.

and the ion equation is given by

$$\frac{\partial n_i}{\partial t} + \frac{E_y}{B}\sin\theta\frac{\partial n_i}{\partial x} - \frac{E_x}{B}\sin\theta\frac{\partial n_i}{\partial y} = 0. \tag{8}$$

They are coupled by the Poisson equation

$$\begin{aligned} \Delta\phi &= \frac{q}{\varepsilon o}[n_e(x, y, t) - n_i(x, y, t)] \\ n_e(x, y, t) &= \int f(x, y, v_\parallel, t)\, dv_\parallel \end{aligned} \tag{9}$$

and the electric field is given by $\mathbf{E} = -\nabla\phi$.

The characteristics of Eq. (7) are

$$\dot{x} = v_\parallel \cos\theta + E_y \sin\theta/B \tag{10a}$$

$$\dot{y} = -E_x \sin\theta/B \tag{10b}$$

$$\dot{v}_\parallel = -qE_x \cos\theta/m. \tag{10c}$$

Dividing Eq. (10b) by Eq. (10c), we arrive at the desired invariant,

$$I = v_\parallel - \frac{\omega_e}{\tan\theta}y, \tag{11}$$

where $\omega_e = qB/m$. It is easy to recognize that I, multiplied by the electron mass, is nothing but the z component of the canonical momentum $\mathbf{P} = m\mathbf{v} - q\mathbf{A}$, which is conserved since the Hamiltonian does not depend on z.

Now, we pass from the phase space $(x, y, v_\parallel)$ to the new phase space (x, y, I), by defining $f(x, y, v_\parallel, t) = F(x, y, I, t)$. F obeys the equation

$$\begin{aligned} \frac{\partial F}{\partial t} + \left(I\cos\theta + \omega_e\frac{\cos^2\theta}{\sin\theta}y + \frac{E_y}{B}\sin\theta\right)\frac{\partial F}{\partial x} \\ - \frac{E_x}{B}\sin\theta\frac{\partial F}{\partial y} = 0, \end{aligned} \tag{12}$$

where I is now but a continuous label. If we take only a finite number of discrete values of I, we arrive at the set of equations for $F_j(x, y, t) = F(x, y, I_j, t)\,\Delta I$,

$$\begin{aligned} \frac{\partial F_j}{\partial t} + \left(I_j\cos\theta + \omega_e\frac{\cos^2\theta}{\sin\theta}y + \frac{E_y}{B}\sin\theta\right)\frac{\partial F_j}{\partial x} \\ - \frac{E_x}{B}\sin\theta\frac{\partial F_j}{\partial y} = 0 \end{aligned} \tag{13}$$

for $j = 1, N$. Equation (13), together with Eq. (8) for the ions, and the Poisson equation (9), constitute the mathematical model that we shall solve numerically. Note that the Jacobian of the transformation from the old phase space to the new one is equal to one and, therefore,

$$\iiint f(x, y, v_\parallel, t)\, dx\, dy\, dv_\parallel = \iiint F(x, y, I, t)\, dx\, dy\, dI.$$

Furthermore, the electron density is now defined as

$$n_e(x, y, t) = \int F(x, y, I, t)\, dI = \sum_j F_j(x, y, t). \tag{14}$$

The advantage of solving Eq. (13), instead of Eq. (7), is clear: we have replaced a three-dimensional phase space with a countable set of two-dimensional phase spaces. Equation (13) has the same structure as the hydrodynamic equation for the ions, Eq. (8): in a sense, our model represents a $N + 1$ species hydrodynamics. We could have considered kinetic effects for the ions, too, thus arriving at an equation similar to Eq. (13); as we had anticipated, Eq. (8) is recovered in the limit of the ion cyclotron frequency $\omega_i \to 0$, keeping only the invariant $I = 0$.

We stress that the fact of taking a finite number of invariants is not a numerical approximation in the usual sense, but only a particular choice of the initial condition. For instance, let us consider the total energy, which in the old variables reads as

$$\frac{\varepsilon_o}{2}\iint E^2\, dx\, dy + \iiint f_e(x, y, v_\parallel, t)\frac{mv_\parallel^2}{2}\, dx\, dy\, dv_\parallel$$

and which is, of course, conserved. Now, the discrete system constituted of Eqs. (8), (9), (13), and (14) does not destroy the energy conservation, which is now written

$$\begin{aligned} \frac{\varepsilon_o}{2}\iint E^2\, dx\, dy + \frac{m}{2}\sum_{j=1}^{N}\iint F_j(x, y, t) \\ \left(I_j + \frac{\omega_e}{\tan\theta}y\right)^2 dx\, dy = \text{const.} \end{aligned} \tag{15}$$

The constancy of this expression is explicitly shown in Appendix A.

The numerical scheme is based on a splitting algorithm (see Refs. [1, 2]), in which we separate the integration along the x and y directions, according to the sequence of operators: $\hat{X}/2 \cdot \hat{Y}/2 \cdot \hat{P} \cdot \hat{Y}/2 \cdot \hat{X}/2 \cdot \hat{P}$, where $\hat{X}$ and $\hat{Y}$ denote shift operators for half a time-step (hence the factor $\frac{1}{2}$). $\hat{P}$ denotes symbolically that at this point we solve the Poisson equation and calculate the electric fields. This sequence of operators is valid for both ions and electrons, since their evolution equations have the same structure. For example, for the electrons, the solution of Eq. (13) involves the following steps:

(A1) Between t_n and $t_{n+1/2}$ the distribution function $F_j(x, y, t)$ is shifted in x-space for a time $\Delta t/2$ to give $F_j^*(x, y, t_{n+1/2})$

$= F_j(x - \delta x, y, t_n)$, where

$$\delta x = \left(I_j \cos\theta + \omega_e \frac{\cos^2\theta}{\sin\theta} y + \frac{E_y^n}{B} \sin\theta \right) \frac{\Delta t}{2}.$$

In calculating the shift, the electric field is taken at time t_n, which makes the scheme exact only to first order in Δt. However, comparison with a second-order scheme, implemented via a predictor–corrector method, has not shown significant differences for the range of Δt we used.

(A2) We shift F_j along the y-axis for a time $\Delta t/2$, and we obtain

$$F_j(x, y, t_{n+1/2}) = F_j^*(x, y - \delta y, t_{n+1/2}),$$

where $\delta y = -(E_x^n/B) \sin\theta\, (\Delta t/2)$.

(A3) We solve the Poisson equation and calculate the electric fields at time $t_{n+1/2}$.

(A4) We shift again the distribution function F_j in y-space of $\Delta t/2$, yielding

$$F_j^*(x, y, t_{n+1}) = F_j(x, y - \delta y, t_{n+1/2})$$

where $\delta y = -(E_x^{n+1/2}/B) \sin\theta\, (\Delta t/2)$.

(A5) We shift F_j in x-space of $\Delta t/2$ and we get, finally,

$$F_j(x, y, t_{n+1}) = F_j^*(x - \delta x, y, t_n)$$

with

$$\delta x = \left(I_j \cos\theta + \omega_e \frac{\cos^2\theta}{\sin\theta} y + \frac{E_y^{n+1/2}}{B} \sin\theta \right) \frac{\Delta t}{2}.$$

(A6) We again solve the Poisson equation and calculate the electric fields at time t_{n+1}.

This sequence of operations is carried out for each F_j, $j = 1, N$, and for the ion density, according to Eq. (8). Of course, the Poisson equation is solved once for all species. This sequence allows us to push the distribution function from t_n to t_{n+1}. An explicit computation of the shifts requires an interpolation method; we have used a very powerful cubic spline technique, already applied to previous simulations [1, 2, 7, 8]. Note that, with respect to the scheme presented in Ref. [3], our scheme requires four, instead of five, steps to push the distribution function.

The Poisson equation has been solved by taking Fourier transforms in the periodic variable x and using cubic splines for the nonperiodic direction y. Details of the method are given in Refs. [3, 9].

4. NUMERICAL RESULTS FOR THE KH INSTABILITY

When $\theta = 90°$, the dependence on I_j in Eq. (13) disappears, and the dynamical equation for the electrons becomes identical to the one for the ions, Eq. (8). In this case, only the difference of the densities $\rho = n_i - n_e$ intervenes in the equations, which now take the same form of the vorticity equations for an incompressible, inviscid fluid,

$$\frac{\partial \rho}{\partial t} - \frac{\partial \phi}{\partial y}\frac{\partial \rho}{\partial x} + \frac{\partial \phi}{\partial x}\frac{\partial \rho}{\partial y} = 0$$
$$\Delta\phi = -\rho. \tag{16}$$

However, as soon as the magnetic field is tilted ($\theta < 90°$), the entire three-dimensional phase space must be considered. Our expectation is that, for an angle close to 90°, a small number of invariants should be sufficient to reproduce correct results. Note that such "economy" could not have been envisaged for the $v_\parallel$ variable, since numerical differentiation demands a good representation of the function; on the contrary, no numerical differentiation is carried out on the I variable. We can anticipate that the method gives remarkably good results up to $\theta \approx 70°$ and is, therefore, perfectly able to describe the stabilization of the KH instability for decreasing θ. For smaller angles, although the method is, of course, always correct in principle, it becomes as costly as the ordinary eulerian code of Ref. [3]. This fact is due to the choice of the initial condition, which we want to be maxwellian in $v_\parallel$,

$$f(x, y, v_\parallel, t = 0) = n_o(y) e^{-v_\parallel^2/2V_T^2}, \tag{17}$$

where $n_o(y)$ is the profile in the y direction (a sinusoidal perturbation in x space will be added to start up the instability). In the new phase space Eq. (17) becomes

$$F(x, y, I, t = 0) = n_o(y) \exp - \frac{(I + \omega_e y/\tan\theta)^2}{2V_T^2}. \tag{18}$$

Now the maxwellian is centered in the point $I = -\omega_e y/\tan\theta$. For an angle close to 90°, the range of I is mostly determined by the thermal velocity V_T; usually taking an $I_{\max}$ of 3 to 4 V_T is sufficient (note also that the maxwellian can be cut off more abruptly when using the invariant, since no diffusion can take place in I-space). However, when $\omega_e y_{\max}/\tan\theta \geq V_T$, the range of I must be chosen accordingly, for example, $I_{\max} = \omega_e y_{\max}/\tan\theta + 3V_T$. For low θ, this results, of course, in the necessity of keeping more and more labels for the invariant.

We now present the numerical results for the KH instability. In the simulation we adopted the following normalization space is normalized to the electron Debye length $\lambda_{De} = (\varepsilon_o kT_e/ne^2)^{1/2}$; time is normalized to the inverse electron plasma frequency $\omega_{pe}^{-1} = (\varepsilon_o m_e/ne^2)^{1/2}$; velocity is normalized to the electron thermal velocity $V_T = \lambda_{De}\omega_{pe}$.

We chose the initial condition for the two species,

$$f_e(x, y, v_\parallel, t = 0) = \frac{1}{\sqrt{2\pi}} [N(y) + N_b(y)] e^{-v_\parallel^2/2} (1 + \varepsilon \sin k_x x)$$
$$n_i(x, y, t = 0) = N(y)(1 + \varepsilon \sin k_x x), \tag{19}$$

where $N(y)$ and $N_b(y)$ are given by

$$N(y) = K[\tanh \beta(y - y_1) + \tanh - \beta(y - y_2)]$$
$$N_b(y) = \alpha \cdot \operatorname{sech}(y/a). \tag{20}$$

The parameters appearing in Eqs. (19) and (20) have the following values: $\beta = 1.5$; $y_1 = -y_2 = 6.5\ \lambda_{De}$; $\varepsilon = 0.1$; $a = 0.9$. Furthermore, K and α are chosen so that

$$\frac{1}{2L_y} \int_{-L_y}^{L_y} N(y)\, dy = 1$$
$$\frac{1}{2L_y} \int_{-L_y}^{L_y} N_b(y)\, dy = 0.15.$$

Computational parameters are: $L_x = 40\lambda_{De}$, $L_y = 10\lambda_{De}$, $\Delta t\, \omega_{pe} = 0.05$, and $\omega_e/\omega_{pe} = 1$. The number of points $N_x = 64$, $N_y = 80$ will be kept fixed, whilst we shall vary the number of labels N_l. Our main concern will be that of determining I_{max} and N_l for which the numerical solution has converged to some limit, independently of both these quantities.

Figures 2a and 2b show the first and second mode of the potential $|\phi_k|$ as functions of time, in the case $\theta = 89°$: Fig. 2a has been obtained with $N_l = 7$ and $I_{max} = 2.5$; Fig. 2b with $N_l = 31$ and $I_{max} = 5$. We note that the two graphs are strictly identical, proving that seven labels are perfectly able to describe the KH instability correctly. Here and in the following the evolution of the potential harmonics are plotted on a logarithmic scale in base e. The plot shown in Fig. 2a (and the corresponding plot for the case $\theta = 80°$, to be shown in Fig. 5a) are to be compared with the results in Fig. 10 of Ref. [3], which were obtained with another Vlasov code (which does not use the invariant method we present here). Apart from a numerical factor due to the different normalization of the Fourier transform, the curves are in very good agreement. In addition, the code of Ref. [3] had been tested in the case of a sinusoidal profile showing very good agreement with the results of linear theory. This makes us confident that the present code behaves correctly with respect to linear analysis predictions. Countour plots of the electron density and of the electric potential are shown respectively in Fig. 3 and Fig. 4, which were obtained with $N_l = 7$. The same contour plots, obtained with $N_l = 31$ do not show any discrepancy even in the finest details of the density. The typical vortex structures are very well reproduced. Note that the noise visible in Fig. 3b is due to the finite grid resolution and not to the limited number of invariants.

For $\theta = 80°$ we present a more detailed comparison. Three simulations were performed, respectively taking $N_l = 31$ and $I_{max} = 6$, $N_l = 11$ and $I_{max} = 4$, $N_l = 5$ and $I_{max} = 4$. Results for the potential modes are shown in Fig. 5a ($N_l = 31$), Fig. 5b ($N_l = 11$) and Fig. 5c ($N_l = 5$). The first two plots are identical, proving that convergence has been already reached

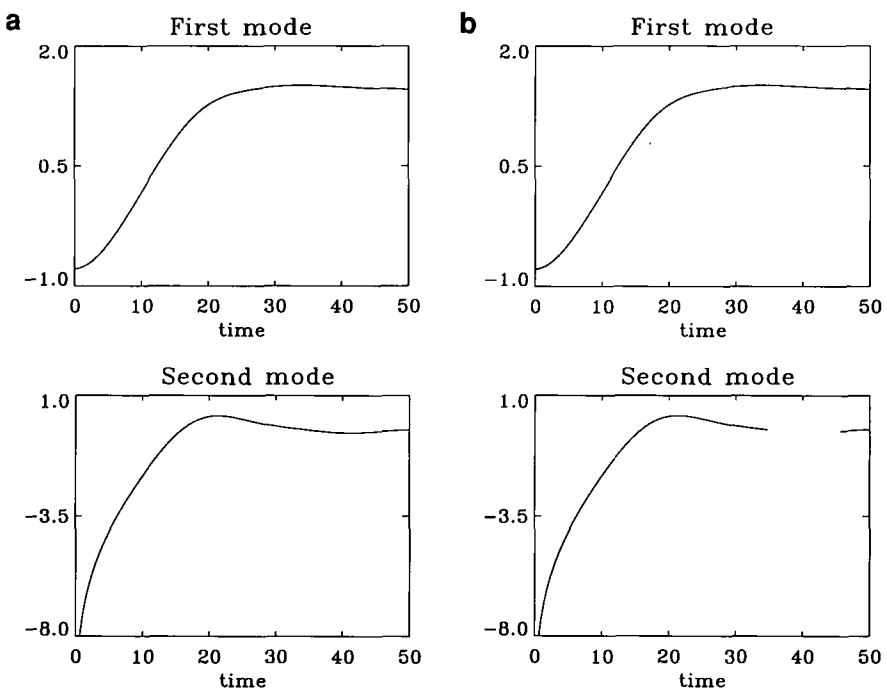

FIG. 2. First and second modes of the electric potential in logarithmic scale for the case $\theta = 89°$: (a) $N_l = 7$; (b) $N_l = 31$.

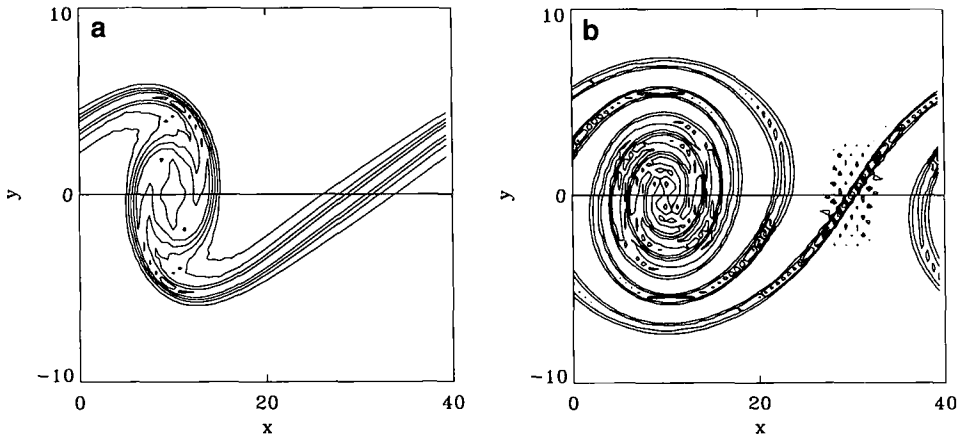

FIG. 3. Contour plot of the electron density, $\theta = 89°$ at (a) $t = 20$, (b) $t = 40$.

for $N_I = 11$, whereas the discrepancies shown in the third one reveals that five labels are not sufficient to describe correctly the evolution. Contour levels of the electron density are shown in Figs. 6, 7, and 8, for the three cases, respectively. Again, the first two figures prove the convergence for $N_I = 11$. Note the formation of a two-vortex structure, which explains the more rapid growth of the second mode of the potential. The electric potential contours are shown in Figs. 9, 10, and 11 at $t = 40$. Again, Figs. 9 and 10 are almost identical.

A further physical insight can be achieved by looking at the distribution function for different values of the invariant. We have done this for the case $\theta = 80°$ and present the results in Figs. 12, 13, and 14. We had for that case $I_{max} = 4$ and $N_I = 11$, thus $\Delta I = 2$, $I_{max}/(N_I - 1) = 0.8$, and $I_j = -I_{max} + (j - 1)\,\Delta I$. In Fig. 12 we show the countour plots of $F(x, y, I)$ for $I = 0$; in Fig. 13, for $I = 1.6$; and in Fig. 14, for $I = 3.2$. The case of $I = 0$ still proves to be unstable, and a two-vortex is clearly visible, whereas for $I = 3.2$ no instability appears.

The conclusion we can draw from the simulations presented in this section is that the KH instability can be reproduced by using a relatively small number of labels. Even when parallel kinetic effects become important, leading to the stabilization of the KH model, only nine labels have proven to be sufficient to describe it correctly. The surprising accuracy and rapid convergence of the method is doubtless due to the fact that the KH instability is essentially a hydrodynamic instability, on which parallel kinetic phenomena act as a small disturbance.

5. SIMULATION OF THE ION-TEMPERATURE-GRADIENT INSTABILITY

Recently, ITG instabilities have been the object of a considerable amount of work [4, 10]; they are believed to play a determinant role in anomalous transport in tokamaks and edge turbulence. These are electrostatic, low frequency waves, which become unstable when the parameter $\eta = d(\ln T_i)/d(\ln n_i)$ exceeds a critical value, usually estimated to be around 2. Their growth rate being very low, simulations with particle codes are

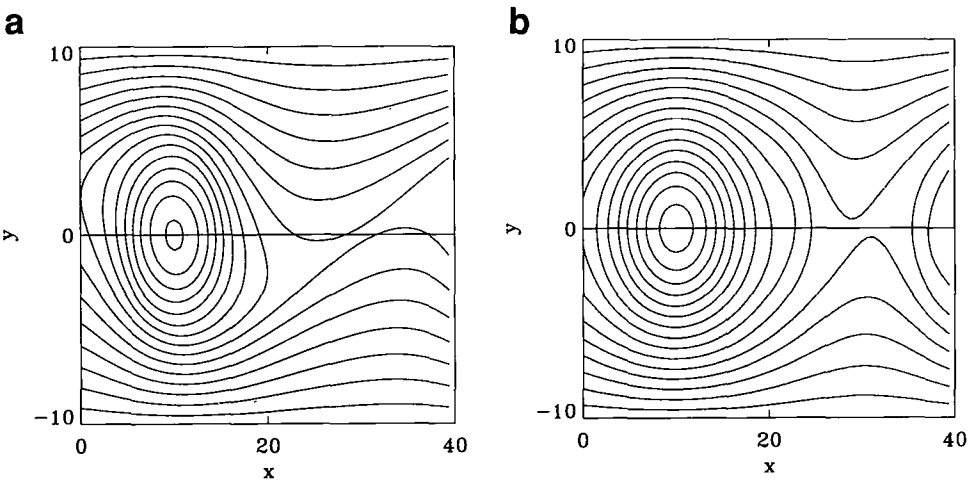

FIG. 4. Contour plot of the electric potential, $\theta = 89°$ at (a) $t = 20$, (b) $t = 40$.

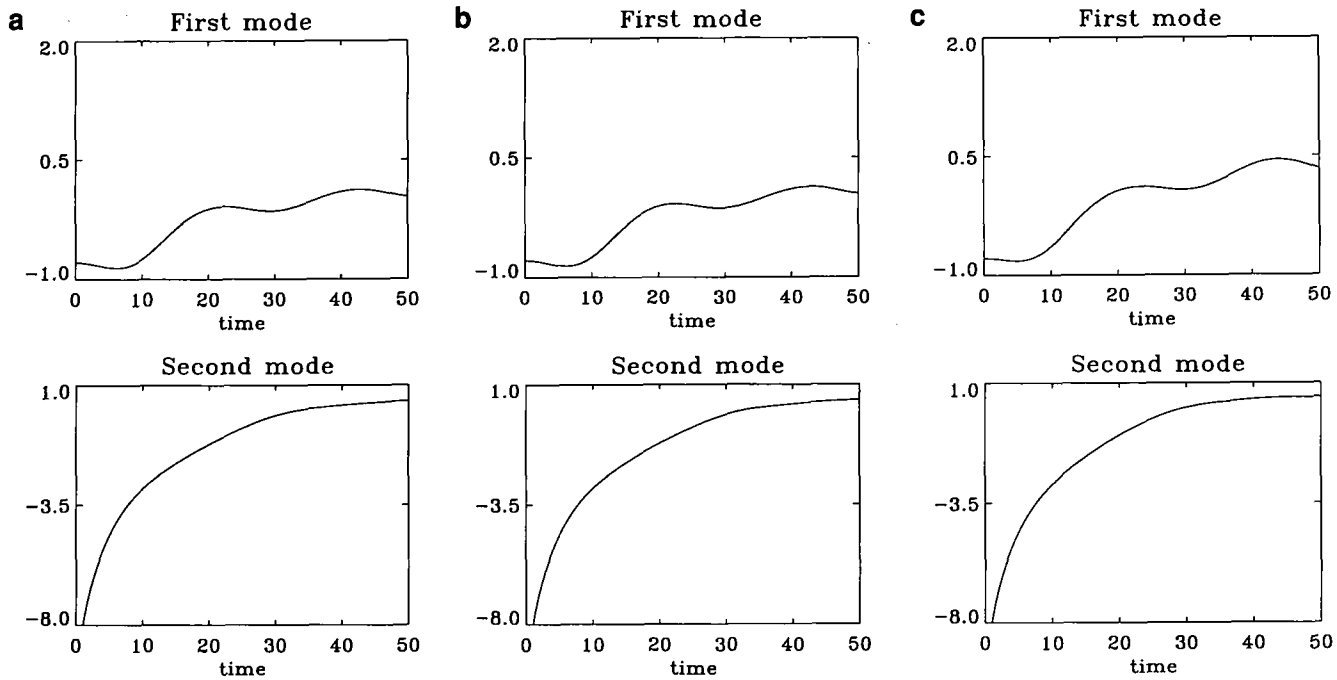

FIG. 5. First and second modes of the potential in logarithmic scale, $\theta = 80°$; (a) $N_t = 31$; (b) $N_t = 11$; (c) $N_t = 5$.

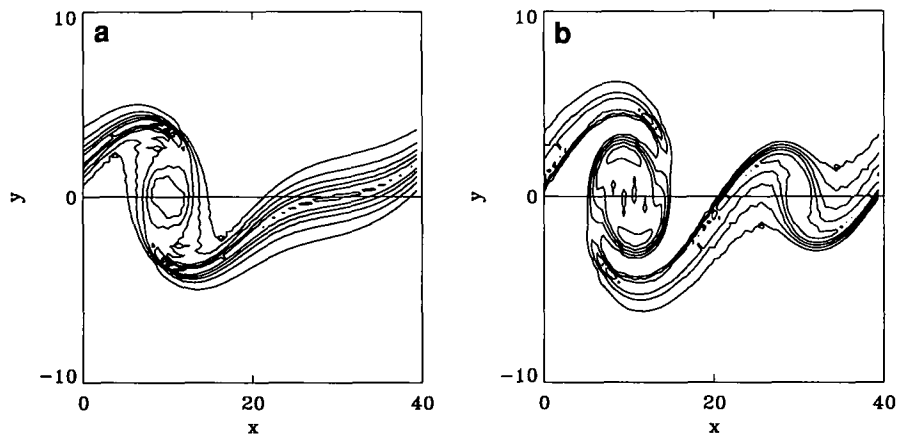

FIG. 6. Contour plot of the electron density for the case $\theta = 80°$, $N_t = 31$ at (a) $t = 30$, (b) $t = 40$.

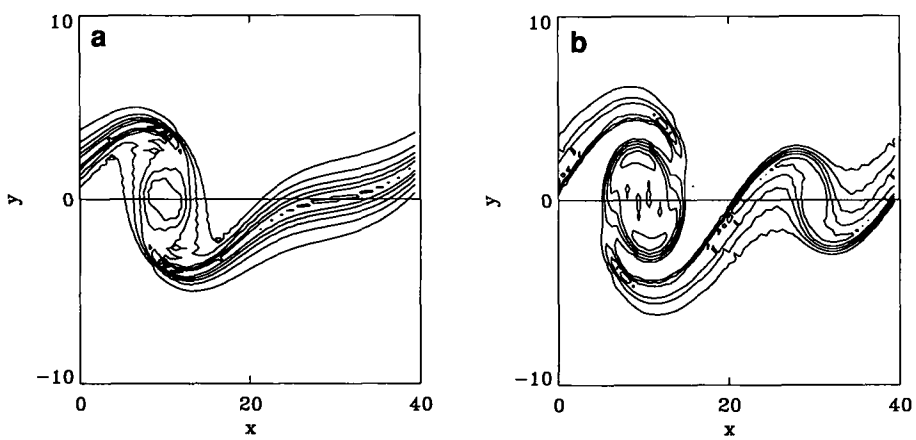

FIG. 7. Same as Fig. 6 for $N_t = 11$ at (a) $t = 30$, (b) $t = 40$.

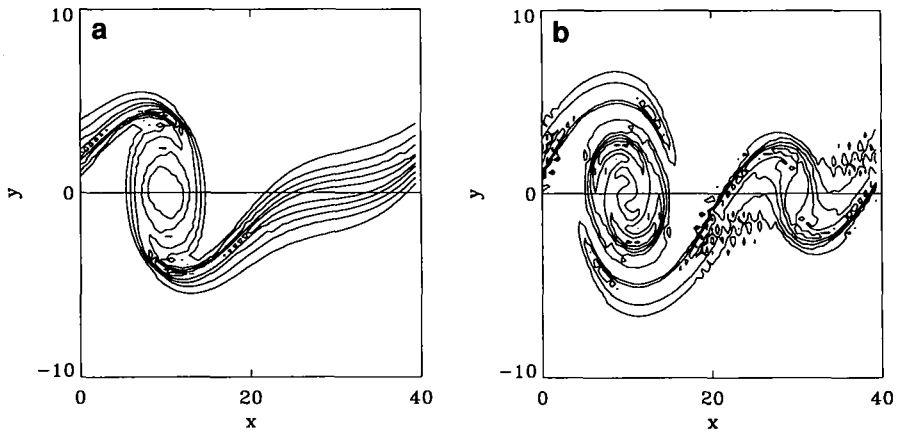

FIG. 8. Same as Fig. 6 for $N_l = 5$.

difficult and display a high noise level. A numerical simulation was carried out with a Vlasov code in Ref. [3], and the linear growth and subsequent non-linear saturation of the instability was shown very clearly. The model used here is slightly different from the previous one for the KH instability. The ions are modeled by the drift-kinetic Vlasov equation (Eq. (6) with the appropriate values of q and m), while the electrons are assumed to follow an adiabatic law. The same bidimensional slab geometry is used. The invariant is now $I = v_\parallel + \omega_i y/\tan\theta$, with $\omega_i = qB/m_i$.

The simulation we present here was done with the initial density and temperature profiles,

$$T_i = T_o(0.2 + 0.8e^{-\beta y^2}), \quad \text{with } T_o = 1,$$
$$n_o = \sqrt{\alpha/\pi}e^{-\alpha y^2}, \quad \text{with } \alpha = 0.025, \beta = 7\alpha,$$

which corresponds to a maximum value $\eta = 5.2$. The initial ion distribution function is then given by

$$f(x, y, v_\parallel, t = 0) = \frac{n_o}{\sqrt{2\pi T_i}} \exp\left(-\frac{v_\parallel^2}{2T_i}\right)$$
$$(1 + \varepsilon \sin k_o x + \varepsilon \sin 2k_o x + \varepsilon \sin 3k_o x)$$

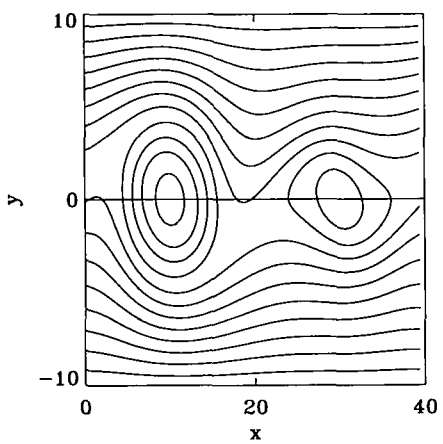

FIG. 9. Contour plot of the potential for the case $\theta = 80°$, $N_l = 31$.

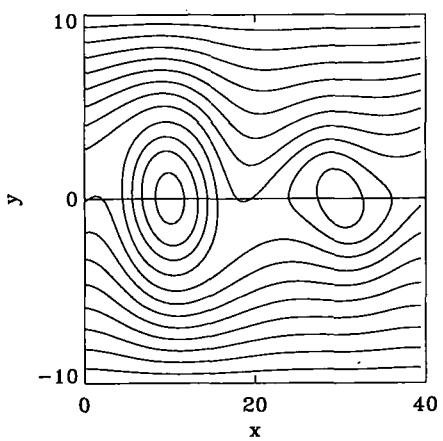

FIG. 10. Same as Fig. 9 for $N_l = 11$.

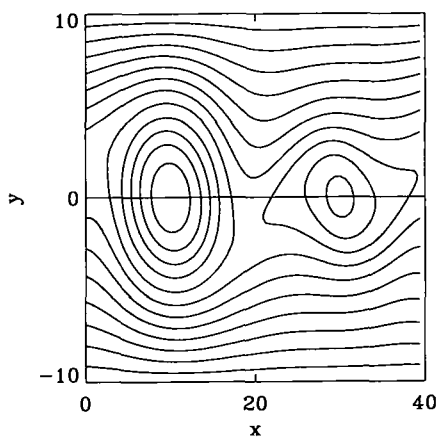

FIG. 11. Same as Fig. 9 for $N_l = 5$.

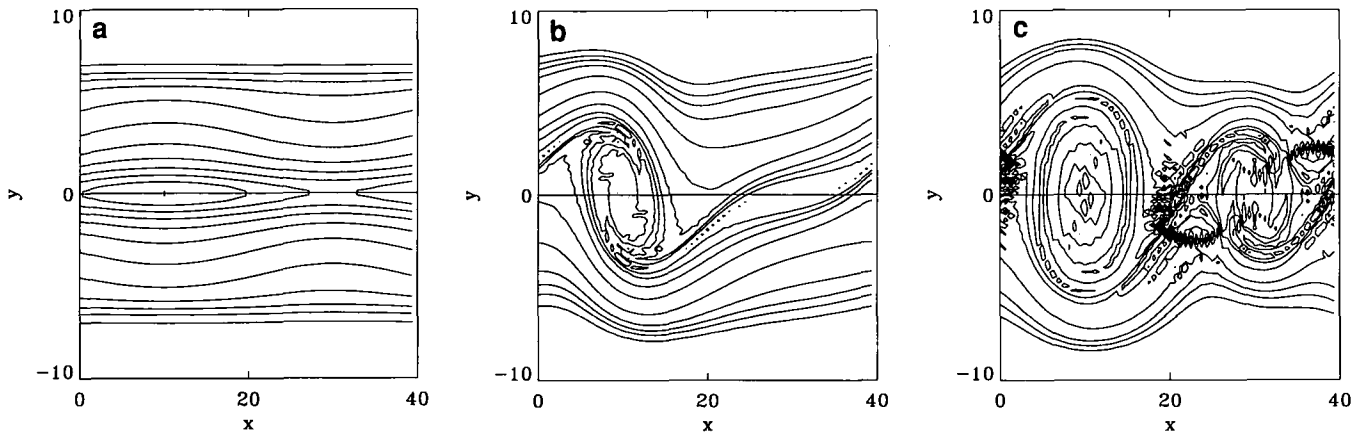

FIG. 12. Contour plot of the distribution function $F(x, y, I_j)$ for $I_j = 0$, $\theta = 80°$, $N_t = 11$, $I_{max} = 4$ at (a) $t = 0$, (b) $t = 30$, and (c) $t = 50$.

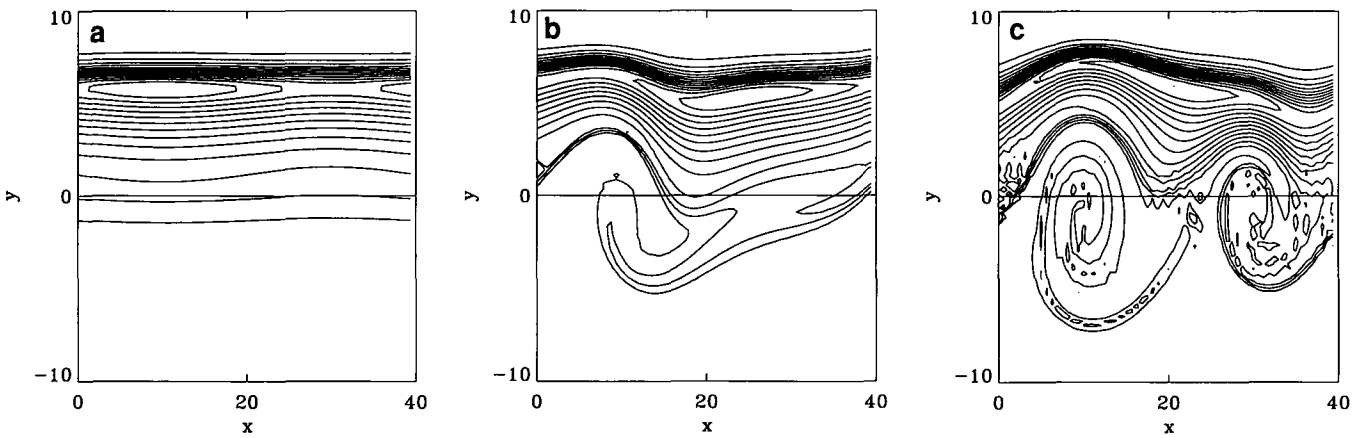

FIG. 13. Same as Fig. 12 for $I_j = 1.6$.

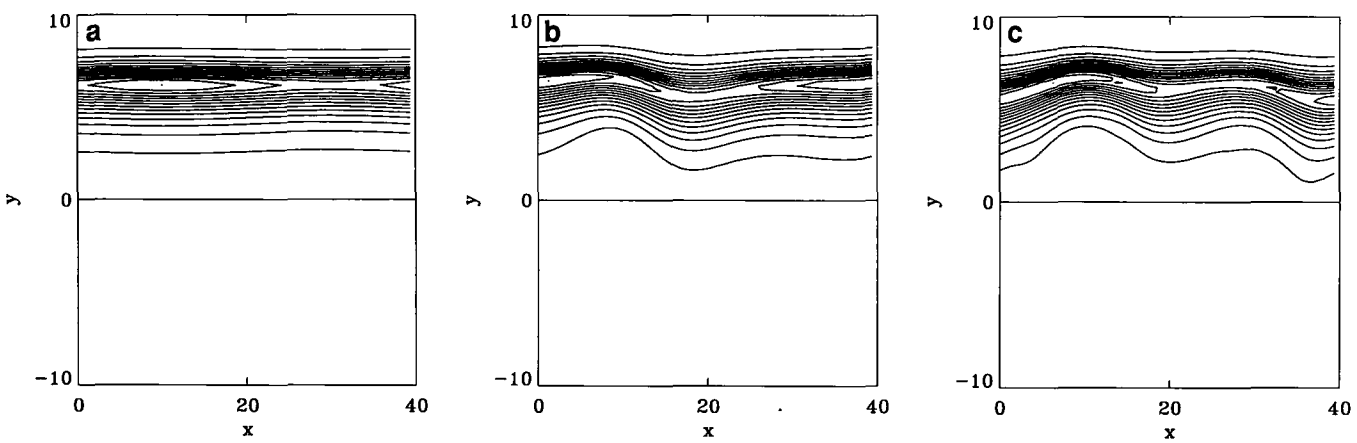

FIG. 14. Same as Fig. 12 for $I_j = 3.2$.

in which $\varepsilon = 0.001$. The velocity variable is normalized to the ion sound speed $C_s = \sqrt{T_e/m_i}$, the space variables are normalized to C_s/ω_{pi}, and time is normalized to ω_{pi}^{-1}. In the Poisson equation, electrons are taken to follow the adiabatic law,

$$n_e(x, y) = n_o(y)(1 + e\phi/T_e),$$

with $T_e = T_o = 1$. The simulation was performed with $\omega_i/\omega_{pi} = 0.5$, $L_x = 32$, and $L_y = 16$, $N_x = 64$, $N_y = 128$, $\omega_{pi}\Delta t = 1$, $\theta = 87°$.

We can expect a priori that the simulation of ITG modes will require a larger number of invariants than we found in the previous examples. In fact, the effect that starts up the ITG instability is of a kinetic, rather than hydrodynamic, nature. Therefore it cannot be viewed as a small perturbation of a hydrodynamic instability; actually, for $\theta = 90°$, the instability disappears. It is equally obvious that we need a sufficient number of points in order to correctly describe the temperature gradient profile. However, an advantage of the present method still comes from the fact of having to solve a partial differential equation in two, rather than three, variables. In addition, as we will show in the next section, a version of such codes for parallel machines is easy to conceive and implement.

We now present the results of a simulation for which we took $I_{max} = 3.6$ and $N_I = 100$. Note that the distribution function can be cut off quite abruptly in the I variable, since it implies no differentiation; we checked that this value of I_{max} is indeed sufficient by taking larger values at equal ΔI.

In Fig. 15a we show the fundamental mode ($k_o = 2\pi/L_x$) of the electric potential as a function of time. The growth rate and the final saturation level are low, which is a good illustration on how the present method can simulate low level instabilities. As a comparison, we report the same plot obtained with $N_I = 50$, and the same I_{max} in Fig. 15b; note that the results are qualitatively in quite good agreement.

Figure 16 shows the contour plot of the electric potential at different times. Complicated structures are formed in the center of the plasma, around $y = 0$. Also, we note a certain symmetry with respect to the straight line $y = 0$. This symmetry is even more evident in the plot of the potential averaged on the x direction, which is shown in Fig. 17. Around $t = 8000$ a structure formed of one "bump" in the center surrounded by two "holes" starts appearing. Note, however, that the potential remains at low levels (the condition $\phi \ll T_e = T_o = 1$ is, in fact, a necessary condition for the consistency of our adiabatic assumption).

The ion and electron density, averaged along the x direction, are plotted in Fig. 18 at $t = 0$ and $t = 14000$. The ion density has undergone a small change, getting slightly higher in the core of the plasma, while the electron density is virtually the same at the beginning and at the end of the evolution. Figure 19 shows the evolution of the net charge density, averaged over the x direction, which develops a profile similar to that of the electric potential.

In order to study how the ITG instability can affect the diffusion of the plasma both in space and velocity space, it is useful to follow the trajectories of test particles. These particles are driven by the electric fields calculated from the Vlasov simulation, but do not contribute themselves to the creation of such fields. So the trajectory and diffusion of these particles can be calculated without any noise. Here we present results for three groups of particles. Particles are initially located between $v = -0.5$ and $v = 0.5$, uniformly distributed in x space and located at different positions in y space, according to each group. Figure 20 shows the (x, y) space for 4096 particles initially situated in the interval $-2 < y < 2$. The diffusion eventually brings some particles quite far from their initial locations. In Fig. 21 we show the evolution of particles initially belonging to the intervals $-4 < y < -2$ and $2 < y < 4$. It is interesting to note that these particles initially located on the slope of the density profile, seem to diffuse more rapidly towards the interior of the plasma than towards the exterior. This is even more evident from the evolution of the third group of 2048 particles (Fig. 22), initially located further down the density profile, between $y = 4$ and $y = 6$. This behavior can be explained by the strong potential gradient experienced by these particles, as shown in Fig. 17.

Figures 23, 24, and 25 show the evolution of each group of particles in the (y, v) space. The existence of an invariant is

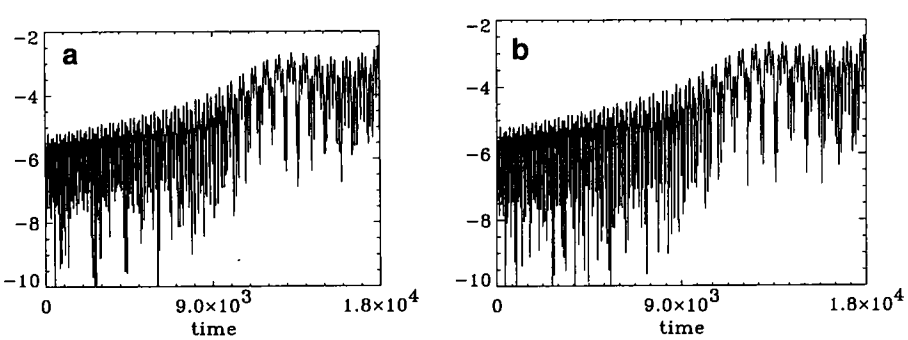

FIG. 15. First mode of the electric potential obtained with (a) $N_I = 100$ or (b) $N_I = 50$ invariants for an ITG instability.

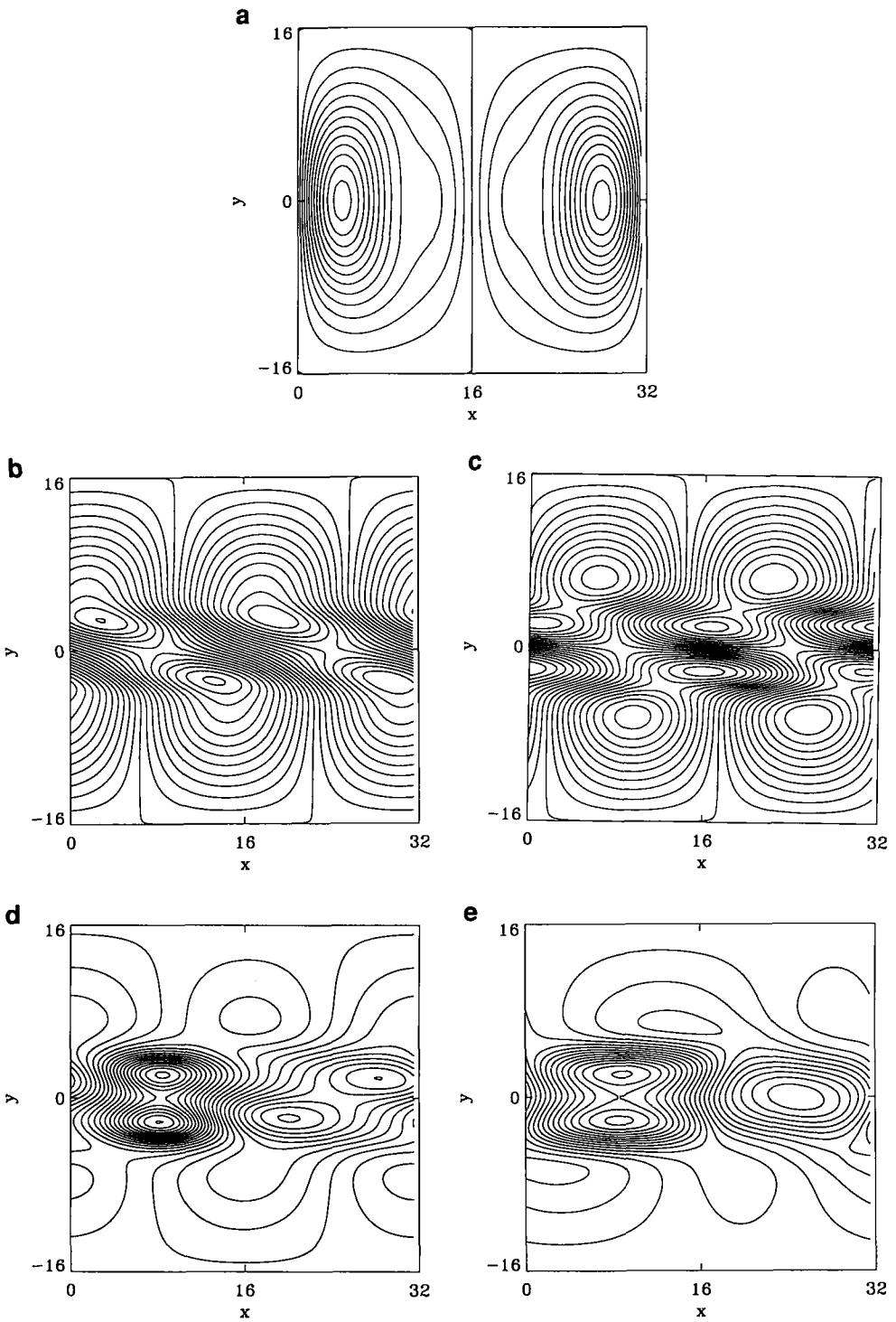

FIG. 16. Contour plot of the electric potential at (a) $t = 0$, (b) $t = 4000$, (c) $t = 6000$, (d) $t = 10{,}000$, and (e) $t = 14{,}000$.

very clear from these figures; the particles move on the straight line $v_\parallel + \omega_i y/\tan\theta = I = \text{const}$. Since the angle θ is close to 90°, the diffusion in velocity space is much slower (of a factor $\omega_i/\tan\theta$) than the diffusion in the y direction.

Finally, we have calculated the quadratic displacements in y and v spaces, Δy^2 and Δv^2, defined as

$$\Delta y^2(t) = \frac{1}{N_{\text{par}}} \sum_{i=1}^{N_{\text{par}}} [y_i(t) - y_i(0)]^2 \tag{21}$$

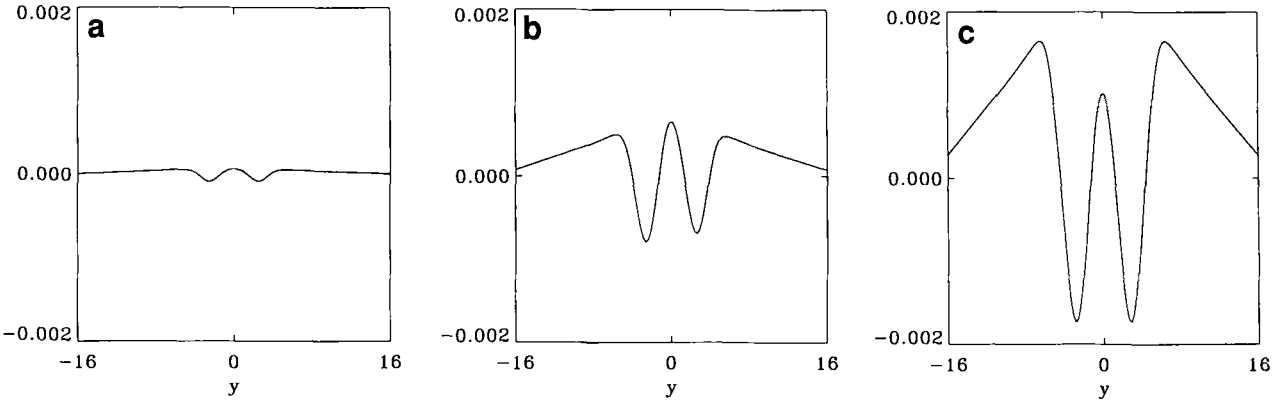

FIG. 17. Profile of the potential, averaged along the x direction at (a) $t = 8000$, (b) $t = 11{,}000$, and (c) $t = 14{,}000$.

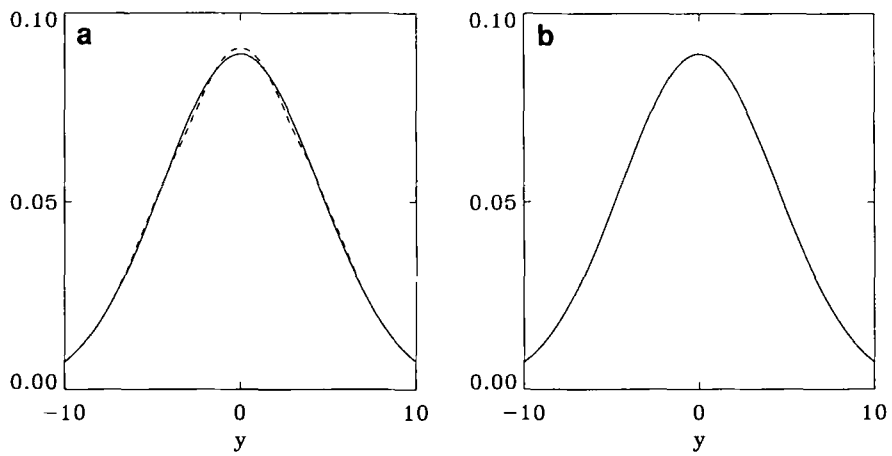

FIG. 18. (a) Averaged ion density profile at $t = 0$ (solid line) and $t = 14000$ (broken line); (b) same as (a) for the electron density.

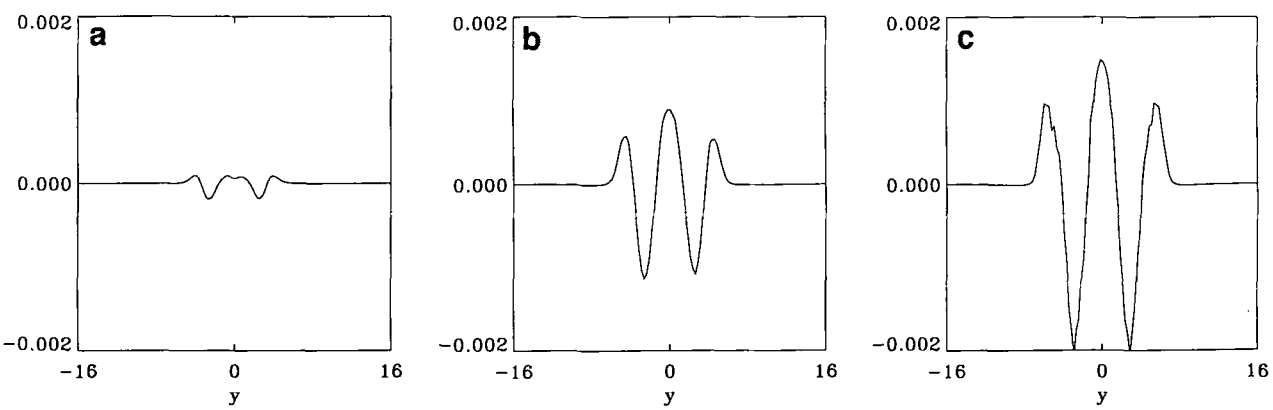

FIG. 19. Profile of the averaged net charge density, averaged along the x direction at (a) $t = 8000$, (b) $t = 11{,}000$, and (c) $t = 14{,}000$.

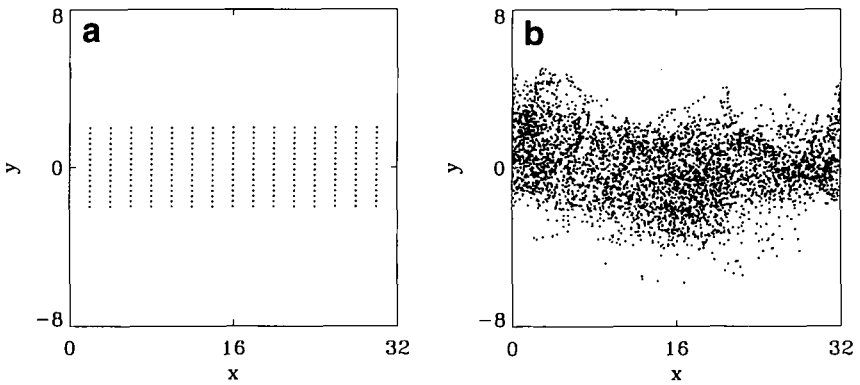

FIG. 20. Evolution in the (x, y) plane of 4096 test particles initially located at $-0.5 < v < 0.5$; $-2 < y < 2$ when (a) $t = 0.0$, and (b) $t = 11{,}000$.

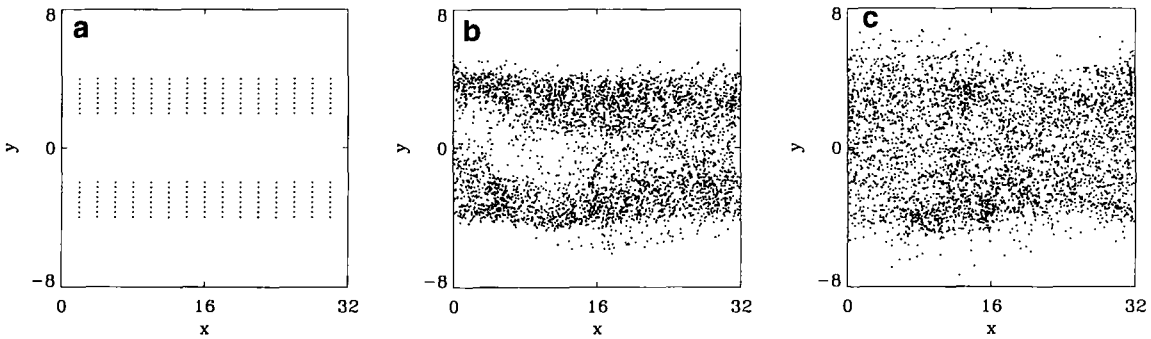

FIG. 21. Same as Fig. 20 for 4096 particles located at $-0.5 < v < 0.5$, $2 < y < 4$, and $-4 < y < -2$ when (a) $t = 0.0$, (b) $t = 11{,}000$, and (c) $t = 14{,}000$.

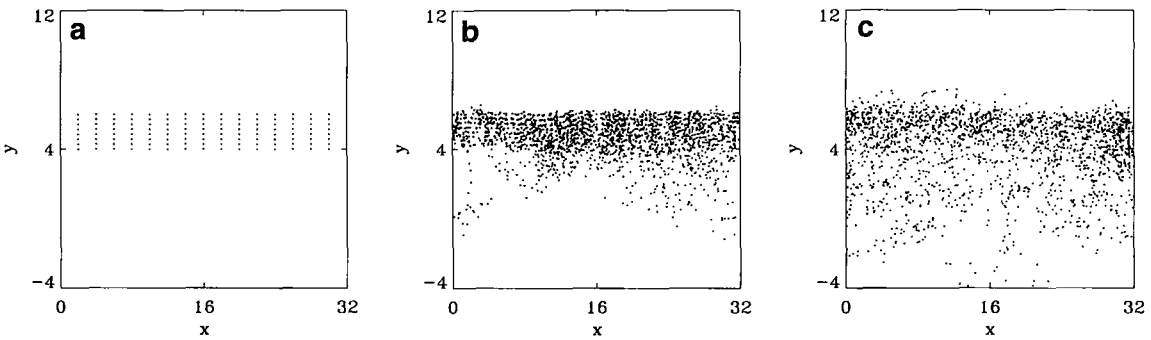

FIG. 22. Same as Fig. 20 for 2048 particles located at $-0.5 < v < 0.5$, $4 < y < 6$ when (a) $t = 0.0$, (b) $t = 11{,}000$, and (c) $t = 14{,}000$.

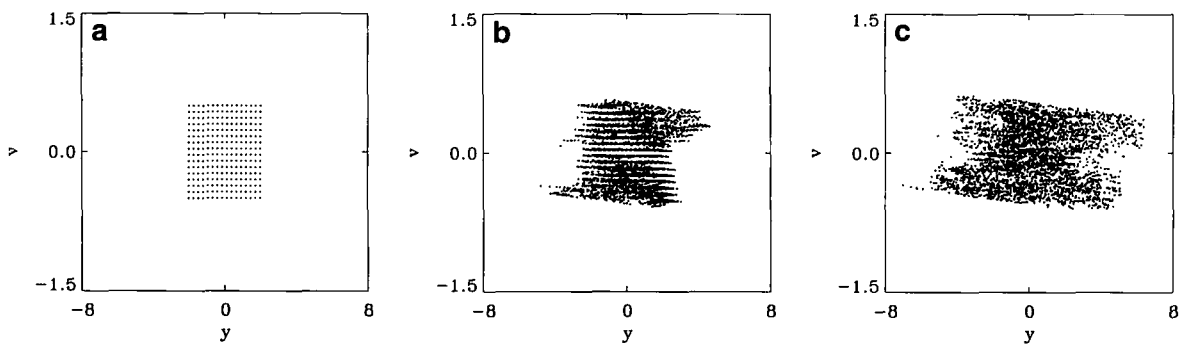

FIG. 23. The same test particles of Fig. 20 represented in the (y, v) space when (a) $t = 0.0$, (b) $t = 10{,}000$, and (c) $t = 14{,}000$.

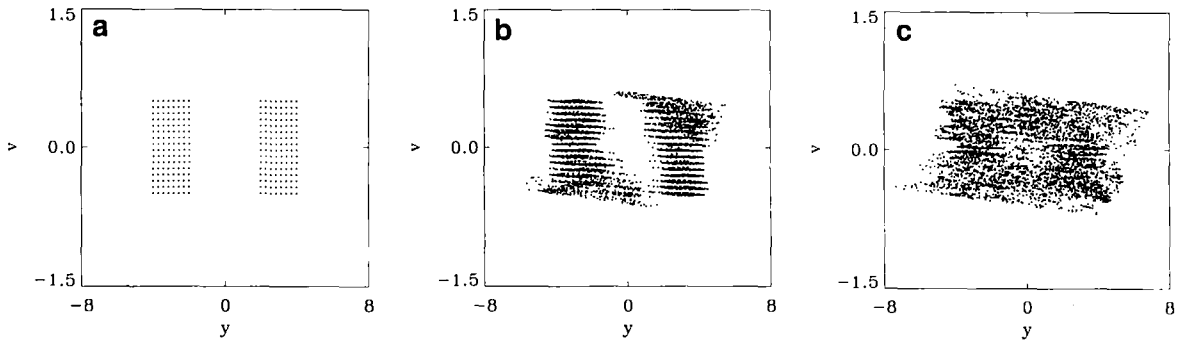

FIG. 24. The same test particles of Fig. 21 represented in the (y, v) space at (a) $t = 0$, (b) $t = 10{,}000$, and (c) $t = 14{,}000$.

with an analogous definition for $\Delta v^2(t)$. These displacements are related to the diffusion coefficients by the relations

$$D_y(t) = \frac{\Delta y^2}{t}, \quad D_v(t) = \frac{\Delta v^2}{t}. \tag{22}$$

Figure 26 shows the time evolution of the quantities Δy^2 and Δv^2 for one group of particles. Note that Δv^2 stays at a very low level: this is due to the fact that the displacements must obey the relation $\Delta v^2/\Delta y^2 = (\omega_i/\tan\theta)^2$, which is a consequence of the existence of an invariant of the motion as previously discussed. So, while the particles are diffusing in space, the diffusion in velocity space is very small. All displacements show a very neat exponential growth and subsequent saturation around $t = 14000$, which follow closely the growth and saturation of the instability, shown in Fig. 15. The initial exponential growth of Δy^2 and Δv^2 is clearly related to the ongoing growth of the instability. In order to eliminate this spurious effect, we divide Δy^2 by the square of the potential amplitude $|\phi_{k_0}|^2$ for the dominant mode k_0. The result is shown in Fig. 27; after a slight increase at the very beginning of the simulation, the curve remains approximately constant.

6. CONCLUSIONS

The aim of this paper was to propose a new technique for the numerical integration of the Vlasov equation, which can be applied whenever the characteristics of the equation possess an exact invariant. By expressing the distribution function in terms of the invariant itself, one can reduce of one unity (or more, if there is more than one invariant) the dimensionality of the pertinent phase space. The invariant enters only as a label in the equations and can therefore be coarsely discretized. We stress once again that the fact of taking a finite and discrete number of invariants is an approximation only in the sense that we choose a very special initial condition: otherwise, since no differential operation is done on the invariant, there is in this respect no other source of numerical errors.

For the drift-kinetic Vlasov equation in a two-dimensional slab geometry, the invariant is nothing but the z component of the canonical momentum. We have studied the KH instability and shown very accurate results with a tilted magnetic field with a small ($\approx$10) number of invariants. The ITG instability was a more challenging problem, since kinetic effects are not negligible even for angles close to 90°. This fact resulted in a larger number of labels of the invariant to be necessary, although qualitative results could be obtained with fewer labels of the invariant.

As we anticipated in the previous section, a version of these codes for parallel machines can be easily implemented. In fact, each of the Eqs. (13), labelled by the index j, evolves independently of all the others. The coupling between the various F_j only intervenes in the Poisson equation. Solving the Eqs. (13)

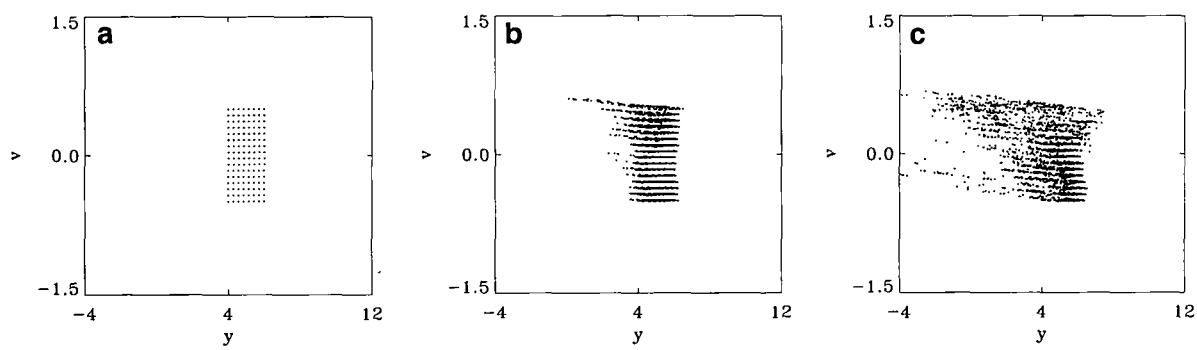

FIG. 25. The same test particles of Fig. 22 represented in the (y, v) space at (a) $t = 0$, (b) $t = 10{,}000$, and (c) $t = 14{,}000$.

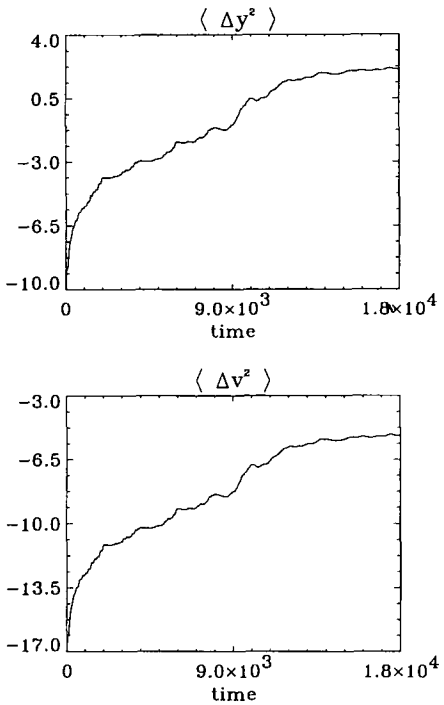

FIG. 26. Evolution of the quantities Δy^2 (higher plot) and Δv^2 (lower plot) for the initial locations $-0.5 < v < 0.5$ and $-2 < y < 2$.

simultaneously on different processors would obviously dramatically decrease the numerical effort. This is a very promising feature of this kind of codes (and, in general, of Vlasov codes) which renders them more attractive on a parallel architecture.

We like to conclude by stating a number of problems that can be attacked through our technique. For a cylindrical plasma column, confined by a magnetic field in the direction of the cylinder axis, an invariant exists if we suppose the plasma to be independent of the azimuthal angle φ. In that case the pertinent phase space is (r, v_r, v_φ) and the invariant is the canonical angular momentum $P_\varphi = mrv_\varphi - qrA_\varphi$, $A_\varphi = -\frac{1}{2}Br$. The v_z velocity, parallel to **B**, could be added without breaking the invariant.

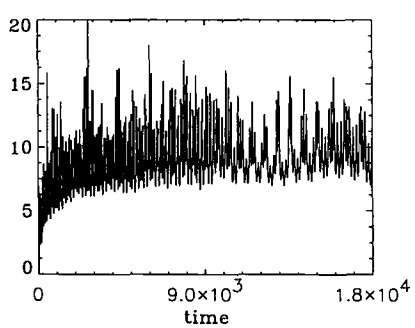

FIG. 27. Evolution of $\Delta y^2/|\phi_{ko}|^2$ for the same group of particles shown in Fig. 26.

In a similar way, in spherical coordinates, a consistent phase space can be spanned by the variables r, v_r, and v_t, the last one being a tangential velocity. Now the invariant is the angular momentum $L = mrv_t$. This model is particularly interesting in stellar dynamics.

Finally, let us consider a relativistic, electrostatic, one-dimensional plasma. The relativistic γ factor depends not only on the longitudinal velocity v_x, but also on the transverse component $v_\perp$. In this case the invariant is the transverse canonical momentum $P_\perp = mv_\perp - qA_\perp$, since it enters the Vlasov equation simply as a continuous label. We plan to address all these issues in future works.

APPENDIX A

In this appendix we prove that the energy theorem for the drift-kinetic Vlasov–Poisson system is valid also when we take a finite and discrete number of invariants.

In the continuum case, given by Eqs. (7), (8), and (9) the total energy is simply:

$$\in = \frac{m}{2}\iiint v_\parallel^2 f(x, y, v_\parallel)\, dx\, dy\, dv_\parallel + \frac{\varepsilon_o}{2}\iint E^2\, dx\, dy. \tag{A1}$$

The discrete model is constituted of Eqs. (8), (13) and the Poisson equation, which reads

$$\Delta\phi = \frac{q}{\varepsilon_o}\left(\sum_j F_j - n_i\right). \tag{A2}$$

We now prove that the expression (A1) becomes

$$\in^* = \frac{m}{2}\sum_j \iint \left(I_j + \frac{\omega_c y}{\tan\theta}\right)^2 F_j(x, y)\, dx\, dy + \frac{\varepsilon_o}{2}\iint E^2\, dx\, dy \tag{A3}$$

and that $\in^*$ is a conserved quantity.

Let us first calculate

$$K = \frac{\partial}{\partial t}\iint \frac{\varepsilon_o}{2} E^2\, dx\, dy. \tag{A4}$$

By making use of the identity $\nabla\cdot(\alpha\mathbf{u}) = \mathbf{u}\cdot\nabla\alpha + \alpha\nabla:\mathbf{u}$ with $\alpha = \phi$ and $\mathbf{u} = \mathbf{E} = -\nabla\phi$ and taking suitable boundary conditions, we have

$$K = -\varepsilon_o \iint \phi\, \Delta\dot{\phi}\, dx\, dy = q\iint \left(\dot{n}_i - \sum_j \dot{F}_j\right)\phi\, dx\, dy,$$

where a dot indicates differentiation with respect to time. Now, by using Eq. (8), it is easy to show that $\iint \phi\dot{n}_i\, dx\, dy = 0$.

Therefore we obtain, through Eq. (13),

$$K = -q \sum_j \iint \phi \dot{F}_j \, dx \, dy$$

$$= q \sum_j \iint \phi \left[\left(I_j \cos\theta + \omega_c \frac{\cos^2\theta}{\sin\theta} y \right) \frac{\partial F_j}{\partial x} + \nabla \cdot (\mathbf{v}_\perp F_j) \right] dx \, dy$$

$$= q \sum_j \iint \phi \left(I_j \cos\theta + \omega_c \frac{\cos^2\theta}{\sin\theta} y \right) \frac{\partial F_j}{\partial x} \, dx \, dy$$

since, again, $\iint \phi \nabla \cdot (\mathbf{v}_\perp F_j) \, dx \, dy = 0$, $\mathbf{v}_\perp = \mathbf{E} \times \mathbf{B}/B^2$. Finally, an integration by parts yields

$$K = q \sum_j \iint \cos\theta \left(I_j + \frac{\omega_c y}{\tan\theta} \right) E_x F_j \, dx \, dy. \tag{A5}$$

Now, multiplying Eq. (13) by $(I_j + \omega_c y/\tan\theta)^2$ and integrating over dx and dy, we get

$$\frac{\partial}{\partial t} \iint F_j \left(I_j + \frac{\omega_c y}{\tan\theta} \right)^2 dx \, dy = -\iint \left(I_j + \frac{\omega_c y}{\tan\theta} \right)^2 \left(I_j \cos\theta + \omega_c \frac{\cos^2\theta}{\sin\theta} y + \frac{E_y}{B} \sin\theta \right) \frac{\partial F_j}{\partial x} \, dx \, dy + \iint \left(I_j + \frac{\omega_c y}{\tan\theta} \right)^2 \frac{E_x \sin\theta}{B} \frac{\partial F_j}{\partial y} \, dx \, dy$$

$$= -2 \frac{q}{m} \cos\theta \iint F_j \left(I_j + \frac{\omega_c y}{\tan\theta} \right) E_x \, dx \, dy. \tag{A6}$$

To obtain the last equality in (A6) we have integrated by parts ($\int E_y (\partial F_j/\partial x) \, dx = -\int F_j (\partial E_y/\partial x) \, dx$, etc.) and made use of the relation $\nabla \times \mathbf{E} = 0 = \partial E_x/\partial y - \partial E_y/\partial x$.

By comparing (A6) with (A5) and remembering the definition (A4), we obtain

$$\frac{\partial}{\partial t} \iint \frac{\varepsilon_0}{2} E^2 \, dx \, dy = -\frac{\partial}{\partial t} \frac{m}{2} \sum_j \iint F_j \left(I_j + \frac{\omega_c y}{\tan\theta} \right)^2 dx \, dy$$

which readily gives the energy theorem (A3).

ACKNOWLEDGMENTS

G. Manfredi acknowledges the hospitality of the CCFM. G. Manfredi and M. Shoucri are grateful to Professor G. Knorr for many fruitful discussions. The CCFM is a joint venture of Hydro-Québec, Atomic Energy of Canada Limited, and the Institut National de la Recherche Scientifique, in which MPB Technologies Inc. and Canatom Inc. also participate. It is principally funded by AECL, Hydro-Québec, and INRS.

REFERENCES

1. C. Z. Cheng and G. Knorr, *J. Comput. Phys.* **22,** 330 (1976).
2. R. R. J. Gagné and M. M. Shoucri, *J. Comput. Phys.* **24,** 445 (1977).
3. A. Ghizzo, P. Bertrand, M. Shoucri, E. Fijalkow, and M. R. Feix, *J. Comput. Phys.* **108,** 105 (1993).
4. Ch. P. Ritz, H. Lin, T. L. Rhodes, and A. J. Woolton, *Phys. Rev. Lett.* **65,** 2543 (1990).
5. H. Biglari, P. H. Diamond, and P. W. Terry, *Phys. Fluids B* **2,** 1 (1990).
6. M. Gros, P. Bertrand, and G. Baumann, *Plasma Phys.* **19,** 811 (1977); M. Feix and P. Bertrand, in *Proceedings, 2nd International Congress on Waves and Instabilities in Plasmas, Institute of Theoret. Phys., Innsbruck University, Innsbruck, 1975,* p. 517.
7. A. Ghizzo, P. Bertrand, M. Shoucri, T. W. Johnston, E. Fijalkow, and M. R. Feix, *J. Comput. Phys.* **90,** 431 (1990).
8. P. Bertrand, A. Ghizzo, T. W. Johnston, M. Shoucri, E. Fijalkow, and M. R. Feix, *Phys. Fluids B* **2,** 1028 (1990).
9. G. Knorr, G. Joyce, and A. Marcus, *J. Comput. Phys.* **38,** 227 (1980).
10. W. W. Lee and W. M. Tang, *Phys. Fluids* **31,** 612 (1988).
11. W. W. Lee, *J. Comput. Phys.* **72,** 243 (1987).